applied sciences

MDPI

Article

Modelling of High-Velocity Impact on Woven Carbon Fibre-Reinforced Plastic Laminate

Nenad Djordjevic [1,*], Rade Vignjevic [1], Kevin Hughes [1] and Tom De Vuyst [2]

[1] Centre for Assessment of Structures and Materials Under Extreme Conditions, Department of Mechanical and Aerospace Engineering, Brunel University of London, London UB8 3PH, UK; v.rade@brunel.ac.uk (R.V.); kevin.hughes@brunel.ac.uk (K.H.)
[2] Materials and Structures Group, University of Hertfordshire, Hatfield AL10 9EU, UK
* Correspondence: nenad.djordjevic@brunel.ac.uk

Abstract: This paper describes a constitutive model for progressive damage in carbon fibre-reinforced composites (CFRPs), developed in the framework of thermodynamics and coupled with a vector equation of state. This made the constitutive model capable of modelling shock wave propagation within orthotropic materials. Damage is incorporated in the model by using reduction in the principal material stiffness based on the effective stress concept and the hypothesis of strain energy equivalence. Damage evolution was defined in terms of a modified Tuler–Bucher criteria. The constitutive model was implemented into Lawrence Livermore National Laboratory (LLNL) DYNA3D nonlinear hydrocode. Simulation results were validated against post-impact experimental data of spherical projectile impact on an aerospace-grade woven CFRP composite panel. Two plate thicknesses were considered and a range of impact velocities above the ballistic limit of the plates, ranging from 194 m/s to 1219 m/s. Other than for the size of the delamination zone in the minor material direction, the discrepancy between the experiments and numerical results for damage and delamination in the CFRP target plates was within 8%.

Keywords: shock wave; impact; damage; composites; hydrocode; FEM

Academic Editors: Spyridon Psarras and Kostopoulos Vassilis

Received: 14 November 2024
Revised: 13 December 2024
Accepted: 18 December 2024
Published: 8 January 2025

Citation: Djordjevic, N.; Vignjevic, R.; Hughes, K.; De Vuyst, T. Modelling of High-Velocity Impact on Woven Carbon Fibre-Reinforced Plastic Laminate. *Appl. Sci.* **2025**, *15*, 555. https://doi.org/10.3390/app15020555

1. Introduction

Across a large number of industrial sectors, composites are the material of choice for the design of lightweight, more energy-efficient and net zero structures, due to their excellent stiffness and strength-to-density ratio. However, the design of composite structures is still limited by the lack of understanding of composite materials, especially their response to high-rate dynamic loading, such as high-velocity impacts, which is important in a number of industrial sectors. For instance, composite materials used in aerospace applications are very often exposed to impact and extreme dynamic loading, including impacts of orbiting particles on spacecraft, ballistic impact on aircraft, foreign object debris impact on jet engines, bird strikes, etc. The complexity of the material response arises primarily from the extreme level of material anisotropy and pronounced heterogeneity. Due to these uncertainties, modern simulation tools are limited in their capability to predict material degradation, its progression and failure. Challenging areas remain in the predictive modelling of the dynamic behaviour of composite structures and materials, including the modelling of damage and failure, such as damage induced by shock wave propagation outside of the impact zone as well as modelling of damage for the purpose of residual strength assessment and for structural health monitoring.

A number of attempts have been made to develop predictive simulation tools. Owing to the brittle properties of composite materials, a number of failure criteria have been developed, including quadratic failure criteria (Tsai-Hill [1] and Tsai-Wu [2]), which are frequently used for analysis of long fibre laminates. Both criteria account for the interactions between different stress components and different failure modes. However, the interactions of the failure modes in the models prevent analysts from identifying the specific failure mode of the composite material. Chang-Chang [3,4] proposed a failure model for transversally isotropic composite material, with different in-plane failure modes. This model is significant and widely used because it is implemented in LS-Dyna [5] and DYNA3D [6], but it is not able to represent the delamination due to the tensile loading. A comprehensive review of the other failure criteria used for modelling composites can be found in [7] and in World-Wide Failure Exercise (WWFE) [8,9]. The latter includes a critical evaluation and validation of the models against the benchmark experiments. The WWFE concluded that a universally robust and accurate model, in all test cases considered, did not exist. The failure models typically set the material constants and stress to zero when the failure criterion is reached and are not capable of modelling progressive damage.

Due to the high level of heterogeneity of composites, one approach for modelling of damage evolution was based on the micromechanical criteria for material constituents (fibres and matrix) and application of a homogenisation technique to the continuum level. The examples for this approach, where the evolution of damage in the material constituents was described on the basis of Continuum Damage Mechanics (CDM) laws, are [8,9]. Other than the CDM models based on homogenisation, a number of authors use continuum evolution laws and experimentally determined the material parameters for the considered composite materials. For instance, Barbero and De Vivo [10] developed a thermodynamically consistent model for elastic damage for fibre-reinforced laminate, where the evolution was controlled by modified Voce law, given in terms of internal variables. A similar approach was used by Hayakawa et al. in [11], Krajcinovic and coworkers in [12], etc.

Models suitable for the analysis of composite structures with progressive damage capabilities are typically based on a continuum damage mechanics approach and account for gradual material deterioration; see, for instance, [13–18], among many others. For instance, progressive damage in [15,16,19,20] was incorporated in terms of damage variables, which affected diagonal members of the compliance tensor, with a separate failure criterion controlling different composite failure modes (Hashin failure criterion for fibres and separate criteria for matrix were used in [20]). There are two Hashin models based on LaRC03 failure criteria [21], with progressive damage models only applicable to the diagonal members of the stiffness tensor. A more general approach was published in [18,22], where separate Hashin-based failure criteria were used for fibre tension and compression, matrix tension and compression as well as fibre–matrix interface failure and interlaminar tension and compression failure. In this model, damage variables are applied to all members of the stiffness tensor. It is also worth mentioning a physically based phenomenological model developed by Puck [23]. This model is developed for the unidirectional composites and very complicated to modify and apply to woven composites. Gosse and co-workers [24,25] developed strain invariant failure theory (SIFT) for modelling damage. The theory was applied in the static analysis of composite materials, where the damage initiation criteria were defined using the critical values of isotropic strain invariants. The use of the strain invariants contributed to the physical significance of the theory, but the criteria had to be calculated/checked in the number of points in the material, which made this approach very tedious and not effective for application in the dynamic problems.

Only a selection of these models is currently available in commercial FEM solvers. One example of such a model is the Chang-Chang Composite Failure Model implemented

in LS Dyna and other FEM code. Nevertheless, a significant constraint of the existing damage models for composites is the lack of capabilities for modelling high-velocity impact, especially for the rates of loading where shock waves are formed and propagate within the composite material.

Shock wave propagation through solids became attractive for a wide community of physicists only in the closing decades of the last century, starting from detailed investigations of the shock response of aluminium alloy 2024 [26]. Work by Butcher [27] and Rubin [28] on 6061-T6 predicted that the spall strength should vary in accordance with the one-dimensional stress yield strength according to orientation, but they concluded that directionality has no significant effect on crack formation. Consequently, the numerical models for modelling shock wave propagation were usually developed for the isotropic material formulation; see, for instance, [28].

A constitutive model, capable of modelling shock wave propagation through a material, comprises two parts: an equation of state (EOS), which determines the material response under compression, and a shear part, responsible for shear deformation. This decomposition is relatively simple for isotropic material, since the spherical part of the stress tensor and strain tensor are co-linear and orthogonal to the deviatoric plane. However, in the case of anisotropic material, orthogonality does not hold, because the spherical component of stress can produce a change in shape—deviatoric strain. The first attempt to solve the problem was by Anderson [29], but the proposal failed to predict material response accurately [30].

Consequently, this paper describes a continuum-based progressive damage model for composite materials where the strength part of the model is coupled with vector equation of state. This makes the model applicable to high-velocity impact problems, where a shock wave is formed and propagates through the material. Orthotropic damage is included in the constitutive model through the damage effect tensor applied on the principal material stiffness and used in the definition of the effective stress, combined with the hypothesis of strain energy equivalence. The evolution equations of the progressive damage model are based on a modified Tuler–Bucher criterion, i.e., time to failure criterion [27,31]. The model was implemented in LLNL Dyna3d explicit hydrocode and our in-house-developed SPH code. The modelling approach was validated in a series of high-velocity impact tests of a hard projectile on an aerospace-grade CFRP composite laminate, where the impact velocities ranged from 194 m/s to 1219 m/s, i.e., all above the ballistic limit of the laminate.

The paper consists of five sections. Following the introduction, the constitutive model is derived in Section 2. An outline of the experimental programme used for the numerical validation is given in Section 3, with the numerical validation for a range of impact cases above the ballistic limit presented in Section 4. Section 5 presents key findings and an outline of future work.

2. Constitutive Model

The constitutive model was developed in the framework of irreversible thermodynamics with internal variables. Based on the evident brittle properties of the composites, the elastic strains were assumed to be small, and the plastic deformation was neglected in the current version of the model. Consequently, energy dissipation of a deformation process is solely driven by damage. This was incorporated in the model as a damage effect tensor operating on the material elastic stiffness tensor (see, for instance, [32,33]). These assumptions significantly simplified the constitutive model formulation and allow for the model to be defined in the current configuration.

Due to the pronounced heterogeneity and anisotropy of composite materials, a number of internal damage parameters need to be defined in order to represent distinct damaging

and failure modes (see, for instance, [34]), such as the tensile damage parameter, the shear damage parameter, the interface damage parameter, etc. The evolution of these parameters is then defined in the separate constitutive laws. This approach is used in the definition of the constitutive model proposed in this work.

Damage in this material model was defined by using the principle of strain energy equivalence, originally derived by Cordebois and Sidoroff [35,36] as a generalization of the pioneering work of Kachanov [37]. A linear relationship between the effective and nominal Cauchy stress was defined by damage effect tensor:

$$\overline{\boldsymbol{\sigma}} = \mathbb{M}(\boldsymbol{\omega}) : \boldsymbol{\sigma} \tag{1}$$

where $\overline{\boldsymbol{\sigma}}$ denotes effective Cauchy stress tensor, which "acts" on the virgin material, and $\mathbb{M}(\boldsymbol{\omega})$ is a fourth-order damage effect tensor, which is a function of a second-order damage tensor $\boldsymbol{\omega}$. The energy equivalence principle produces a similar relationship between the nominal and effective elastic strains, i.e., $\overline{\boldsymbol{\varepsilon}}_e = \mathbb{M}^{-1} : \boldsymbol{\varepsilon}_e$, which, combined with Equation (1), leads to the relationships between the damage stiffness tensor $\mathbb{C}$ and its virgin counterpart, $\overline{\mathbb{C}}$, as:

$$\mathbb{C}(\boldsymbol{\omega}) = \mathbb{M}^{-1}(\boldsymbol{\omega}) \colon \overline{\mathbb{C}} : \mathbb{M}^{-1}(\boldsymbol{\omega}) \tag{2}$$

To maintain symmetry of the effective stress tensor, the damage effect tensor was defined by a product type symmetrisation (see, for instance, [38]), in the following form:

$$\mathbb{M}(\boldsymbol{\omega}) = (\boldsymbol{I} - \boldsymbol{\omega})^{-\frac{1}{2}} (\boldsymbol{I} - \boldsymbol{\omega})^{-\frac{1}{2}} \qquad \mathbb{M}_{\mathrm{ijkl}} = (\delta_{\mathrm{ik}} - \omega_{\mathrm{ik}})^{-\frac{1}{2}} \left(\delta_{\mathrm{jl}} - \omega_{\mathrm{jl}}\right)^{-\frac{1}{2}} \tag{3}$$

which has a diagonal form in the principal directions of damage, where ω_{ik}, $i = k = 1,2,3$ are principal values of the damage tensor. The damage effect tensor given in Equation (3) can now be substituted in Equation (2), leading to the stiffness tensor of a damaged material as:

$$\mathbb{C} = \begin{bmatrix} \mathbb{C}_{11}(1-\omega_1)^2 & \mathbb{C}_{12}(1-\omega_1)(1-\omega_2) & \mathbb{C}_{31}(1-\omega_3)(1-\omega_1) & 0 & 0 & 0 \\ & \mathbb{C}_{22}(1-\omega_2)^2 & \mathbb{C}_{23}(1-\omega_2)(1-\omega_3) & 0 & 0 & 0 \\ & & \mathbb{C}_{33}(1-\omega_3)^2 & 0 & 0 & 0 \\ & & & \mathbb{C}_{44}(1-\omega_2)(1-\omega_3) & 0 & 0 \\ \text{symm} & & & & \mathbb{C}_{55}(1-\omega_1)(1-\omega_3) & 0 \\ & & & & & \mathbb{C}_{66}(1-\omega_1)(1-\omega_2) \end{bmatrix} \tag{4}$$

The stiffness in Equation (4) is used in the definition of Helmholtz free energy and Gibbs energy and further in the definition of the dissipation rate. By making use of the Legendre transformation [38]:

$$\rho g(\boldsymbol{\sigma}, \boldsymbol{\omega}, \theta) = \rho \psi(\boldsymbol{\varepsilon}_e, \boldsymbol{\omega}, \theta) - \boldsymbol{\sigma} : \boldsymbol{\varepsilon}_e \tag{5}$$

and constitutive equation for stress and strain, one can define the Gibbs energy in terms of damage and stress tensors and temperature as:

$$\rho g(\boldsymbol{\sigma}, \boldsymbol{\omega}, \theta) = \frac{1}{2}\boldsymbol{\varepsilon}_e : \quad \mathbb{C} : \boldsymbol{\varepsilon}_e - \boldsymbol{\sigma} : \boldsymbol{\varepsilon}_e = \frac{1}{2}\mathbb{C}^{-1} : \boldsymbol{\sigma} : \mathbb{C} : \mathbb{C}^{-1} : \boldsymbol{\sigma} - \boldsymbol{\sigma} : \mathbb{C}^{-1} : \boldsymbol{\sigma} = -\frac{1}{2}\boldsymbol{\sigma} : \mathbb{C}^{-1} : \boldsymbol{\sigma} \tag{6}$$

The rate of change of Gibbs energy can be obtained as:

$$\rho \dot{g}(\boldsymbol{\sigma}, \boldsymbol{\omega}, \theta) = -\boldsymbol{\varepsilon}_e : \dot{\boldsymbol{\sigma}} - \frac{1}{2}\boldsymbol{\sigma} : \quad \mathbb{M}(\boldsymbol{\omega}) : \overline{\mathbb{C}}^{-1} : \frac{\partial \mathbb{M}(\boldsymbol{\omega})}{\partial \boldsymbol{\omega}} : \boldsymbol{\sigma} : \dot{\boldsymbol{\omega}} + \rho \frac{\partial g}{\partial \theta}\dot{\theta} \tag{7}$$

and further used in the expression for the adiabatic dissipation rate:

$$\begin{aligned}\Delta &= \boldsymbol{\sigma} : \dot{\boldsymbol{\varepsilon}} - \rho\dot{\psi} - \rho\dot{\theta}s = \boldsymbol{\sigma} : \dot{\boldsymbol{\varepsilon}} - \left(\dot{\boldsymbol{\sigma}} : \boldsymbol{\varepsilon}_e + \boldsymbol{\sigma} : \dot{\boldsymbol{\varepsilon}}_e + \rho\dot{g}\right) - \rho\dot{\theta}s = \\ &= -\dot{\boldsymbol{\sigma}} : \boldsymbol{\varepsilon} - \left(-\boldsymbol{\varepsilon}_e : \dot{\boldsymbol{\sigma}} - \tfrac{1}{2}\boldsymbol{\sigma} : \quad \mathbb{M}(\boldsymbol{\omega}) : \overline{\mathbb{C}}^{-1} : \tfrac{\partial \mathbb{M}(\boldsymbol{\omega})}{\partial \boldsymbol{\omega}} : \boldsymbol{\sigma} : \dot{\boldsymbol{\omega}} + \rho\tfrac{\partial g}{\partial \theta}\dot{\theta}\right) - \rho\dot{\theta}s = \\ &= -\left(\rho\tfrac{\partial g}{\partial \theta} + s\right)\dot{\theta} + \tfrac{1}{2}\boldsymbol{\sigma} : \mathbb{M}(\boldsymbol{\omega}) : \overline{\mathbb{C}}^{-1} : \tfrac{\partial \mathbb{M}(\boldsymbol{\omega})}{\partial \boldsymbol{\omega}} : \boldsymbol{\sigma} : \dot{\boldsymbol{\omega}} \geq 0\end{aligned} \tag{8}$$

The first term in the inequality above leads to the constitutive equation for entropy, whilst the latter determines dissipation rate per unit initial volume:

$$s = -\rho\frac{\partial g}{\partial \theta} \qquad \Delta = \frac{1}{2}\boldsymbol{\sigma} : \quad \mathbb{M}(\boldsymbol{\omega}) : \overline{\mathbb{C}}^{-1} : \frac{\partial \mathbb{M}(\boldsymbol{\omega})}{\partial \boldsymbol{\omega}} : \boldsymbol{\sigma} : \dot{\boldsymbol{\omega}} \geq 0 \tag{9}$$

Note from the inequality in (9) that dissipation rate is determined by the rate of change of the damage tensor and a definition of the damage effect tensor. The evolution equations for damage internal variables, which constitute the damage tensor, were defined directly, making use of modified Tuler–Bucher criterion [27,31]. The current development of the constitutive model relates damage in the principal direction to the parameters that control the evolution of the particular damage mode.

Originally, Tuler–Bucher [27] proposed a criterion for failure:

$$\phi = \int_0^{t_{\mathrm{cr}}} f(\sigma(t))dt \tag{10}$$

where f can be any convenient function of stress, usually $(\sigma - \sigma_0)^{\lambda}$; σ_0 is a threshold stress below which no failure occurs, and t_{cr} is time to failure. The method was originally proposed for unidirectional loading. To be applied to the orthotropic material and three-dimensional loading conditions, effective stress was utilised. Delamination was modelled by an in-plane criterion based on the out-of-plane (through thickness) normal stress component. The function $f(\sigma(t))$ was normalised with the corresponding member of the material stiffness matrix, so that evolution of the damage variables was defined as:

$$\dot{\omega} = \dot{\omega}(\omega, \sigma) = \Omega_{\omega}\left(\frac{\sigma}{C_m(1-\omega)} - \frac{\sigma_{\mathrm{cr}}}{C_m}\right)H\left(\frac{\sigma}{C_m(1-\omega)} - \frac{\sigma_{\mathrm{cr}}}{C_m}\right) \tag{11}$$

$$\dot{\omega}_{\mathrm{del}} = \dot{\omega}_{\mathrm{del}}(\omega, \sigma) = \Omega_{\mathrm{del}}\left(\frac{\sigma_{33}}{C_{33}(1-\omega_3)} - \frac{\sigma_{\mathrm{cr_{del}}}}{C_{33}}\right)H\left(\frac{\sigma_{33}}{C_{33}(1-\omega_3)} - \frac{\sigma_{\mathrm{cr_{del}}}}{C_{33}}\right) \tag{12}$$

where Ω_{ω} and Ω_{del} are material parameters determined by time to failure, σ and σ_{33} are effective stress and out-of-plane stress, respectively, σ_{cr} and σ_{crdel} are critical effective stress and critical out-of-plane stress, C_m and C_{33} are maximum in-plane stiffness member and through the thickness coefficient, respectively, H is Heaviside function. The integration of Equations (11) and (12) provides damage internal variables for principal directions of damage, ω_1, ω_2 and ω_3, which are further used for the update of the damaged stiffness tensor in Equation (4). Note that the first two variables correspond to the fibre directions in the woven material, whilst the third is a damage variable for the out-of-plane direction.

The proposed damage model has been implemented into the LLNL code DYNA3D [6] and coupled with an orthotropic elastic constitutive model with vector equation of state (EOS), derived in [30] and outlined below.

The vector EOS defines pressure as a state of stress induced by the volumetric strain only. This physically means that the pressure is a vector in the stress space, which is not collinear with hydrostat, and can be written as:

$$-\hat{P}\psi_{\mathrm{ij}} = C_{\mathrm{ijkl}}\delta_{\mathrm{kl}}\varepsilon_{\mathrm{ss}}/3 = C_{\mathrm{ijkk}}\varepsilon_v \tag{13}$$

where the direction of the pressure in the stress space is defined by tensor ψ_{ij} and volumetric strain is given as $\varepsilon_v = \varepsilon_{ss}/3$. Tensor ψ_{ij} has diagonal members only, so indices in the brackets imply no summation. The governing equations of the decomposition of the stress tensor are summarised below. The first equation in (14) decomposes the stress onto the components $\hat{P}\psi_{ij}$ and $\hat{S}_{ij}$, which are not mutually orthogonal, whilst the second equation in (14) is used in the constitutive model, where the orthogonality between $\widetilde{P}\psi_{ij}$ and $\widetilde{S}_{ij}$ holds. The relationships between the components in Equation (14) are given below; for a detailed derivation, see [30].

$$\sigma_{ij} = -\hat{P}\psi_{ij} + \hat{S}_{ij} = -\widetilde{P}\psi_{ij} + \widetilde{S}_{ij} \tag{14}$$

$$\widetilde{P} = \hat{P} - \frac{\hat{S}_{ij}\psi_{ij}}{\psi_{kl}\psi_{kl}} = \hat{P} - \hat{S} = -\frac{\sigma_{ij}\psi_{ij}}{3} \tag{15}$$

$$\widetilde{S}_{ij} = \hat{S}_{ij} - \frac{\hat{S}_{kl}\psi_{kl}}{\psi_{sr}\psi_{sr}}\psi_{ij} = \hat{S}_{ij} - \hat{S}\psi_{ij} \tag{16}$$

$$\widetilde{S}_{ij} = \sigma_{ij} - \frac{\sigma_{kl}\psi_{kl}}{\psi_{sr}\psi_{sr}}\psi_{ij} = \sigma_{ij} + \widetilde{P}\psi_{ij} \tag{17}$$

The implemented constitutive model was validated against the experiments conducted with woven CFRP, which was modelled with orthotropic material properties, as described in the subsequent sections. However, the model can be applied to the transversally isotropic and isotropic materials, by using appropriate material properties.

3. Experimental Programme

A number of sphere impact tests on woven CFRP plates was carried out at Cranfield Defence and Security Shrivenham [39]. A range of velocities from 179 m/s to 1875 m/s were tested to provide the data for numerical model validation and study the failure mechanisms, specific for composite materials in aerospace applications. Kinetic energy in all considered tests was well above the ballistic limit of the target plates and covers the range of loading conditions where the material undergoes different failure modes, including shock loading. The impact test configuration is shown in Figure 1.

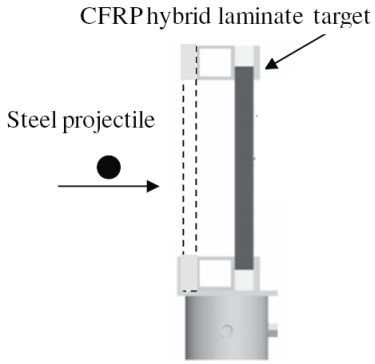

Figure 1. Sphere projectile impact on woven CFRP laminate.

To investigate the effects of the target thickness on the material response to the high-speed sphere impact, two Hexcel composite plates were chosen for the impact trials: a 6 mm thick plate and 12 mm thick plate, which consisted of 16 and 32 plies, respectively. The thinner target plate was made of an asymmetric layup [$0/90$, $\pm 45_2$, $0/90$, $\pm 45_2$,$0/90_2$, $(\pm 45, 0/90)_4$], as shown in Figure 1. The layup effects on the target response and the energy transferred were investigated by impacting the target panels in two normal impact directions. A set of impact cases denoted with A were impacted in the direction denoted in the figure; the impact test performed in the opposite direction was denoted as B. The

simulation programme was focused on the former cases, as the experiments showed that energy transferred to the panel for the range of impact energies 0–500 J (impact velocity from 0 to 375 m/s) was independent of the symmetry of the target plate. The thick panels, denoted as C, were made of two 6 mm panels bonded together by Loctite 0151 (under load for 24 h) to create a symmetric 12 mm thick target plate. These tests aimed to test the thickness effects on the panel response.

In all test cases, the projectile was annealed SS304 stainless steel, 12 mm in diameter (average of Ø11.97 ± 0.1 mm) with a mass of 7.165 g [39]. A detailed metallurgical test of the grain structure of a number of the projectiles used in this experimental work showed that the mechanical properties of the annealed spheres were proven to be isotropic. The yield stress and tensile strength of the material are 450 MPa and 675 MPa, respectively, with the other material properties used in the finite element model are given in Section 4.

The experiments showed that energy transferred to the target increased with the increase in impact energy, which can be attributed to an increased number of damage and failure mechanisms triggered in the composites, such as fibre breakage, fibre pull-out, matrix cracking, matrix crashing, delamination, inelastic deformation of the projectile, etc. A simple calculation showed that over half of the initial kinetic energy was transferred to the particles generated during the penetration of the target, including the remaining kinetic energy of the projectile [39]. More importantly, a change in failure mechanism was observed as a function of the impact velocity, i.e., energy of impact. For a relatively low range of velocities (from 186 m/s to 194 m/s), just above the ballistic limit, material failure started at the rear face of the target and the major failure mechanism was fibre breakage due to the tensile load. The cracking then progressed towards the front face of the target, allowing for the projectile to push the material away and pass through the target. After the projectile had passed through, the previously banded fibres relaxed back to an equilibrium position. As a result, the diameter of the hole made by projectile was significantly smaller than the diameter of the projectile and no plug was formed during the perforation. This type of failure is usually referred to as the petalling type of failure and an image of the rear side of the penetrated target is shown in Figure 2a, whilst the post-impact XCT image of the cross-section through the impact axis is shown in Figure 2b.

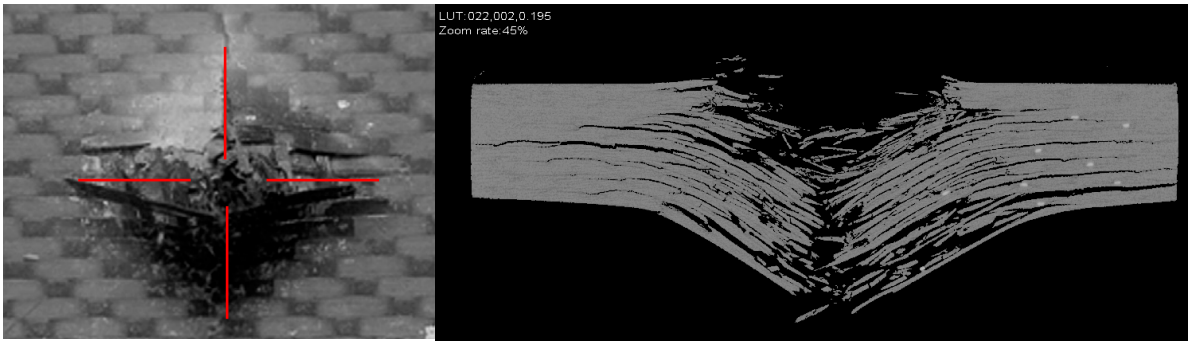

(**a**) (**b**)

Figure 2. (**a**) Rear side of a target CFRP panel impacted at 186 m/s; petalling type of failure with red lines denoting cracks [39] and (**b**) post-impact XCT image of the cross-section of the target.

A change in the failure mechanism was observed at impact velocities above 200 m/s, with the formation of plugs and its size increase with the increase in the impact velocity. For velocities above 300 m/s, a dominant failure mode was shear failure, characterised by conical plug formation and the conical shape of the hole in the target plate. The cross-section of the 6 mm thick target with a conical hole is shown in Figure 3a. Further increase in impact energy (above 500 m/s) led to material failure characterised by a large plume of

dust generated at the rear and the front side of the target. This is due to the shock wave generated at the impact surface and propagated through the material. Due to the radial propagation of shock wave, the material failed on both sides of the target (impact face and rear face), resulting in the hourglass shape of the hole, as shown in Figure 3b).

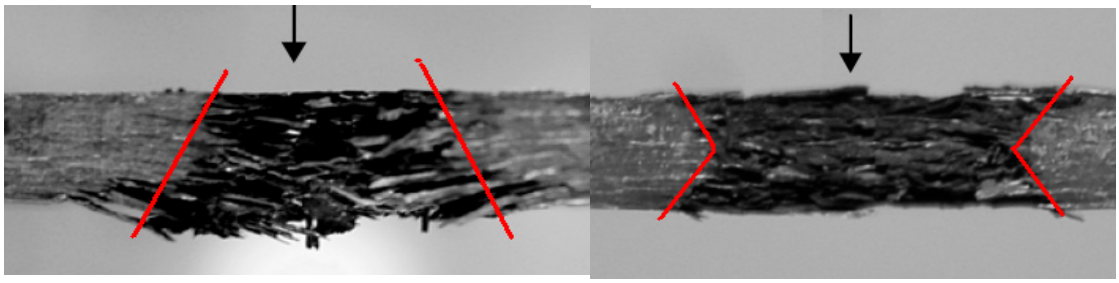

(**a**) (**b**)

Figure 3. Cross-section of a target CFRP panel after the impact with red lines showing the extent of damage: (**a**) impact at 305 m/s; shear-dominated failure and conical shape of the crater [39] and (**b**) impact at 1199 m/s; hourglass shape of the hole [39].

Physical measurements of the panel thicknesses and the damage-related parameters are shown in Table 1. Damage on the impacted and rear face of the 6 mm and 12 mm thick panels (denoted as A3 and C3) is shown in Figures 4 and 5, respectively. The photos illustrate visible delamination and fibre breakage typical of high-velocity impacts on composites.

Table 1. Impact velocities, target thickness, hole dimensions and visible delamination measured in two principal material directions.

					Impact Face		**Rear Face**	
#	**Nominal Velocity, v (m/s)**	**t (mm)**	**x_1 (mm)**	**x_2 (mm)**	**y_1 (mm)**	**y_2 (mm)**	**y_1 (mm)**	**y_2 (mm)**
A-3	1200	6.1	11.7	12.8	19.8	24.3	36.5	23.3
C-3	1219	11.9	11.6	12.8	42.8	35.1	44.6	40.7

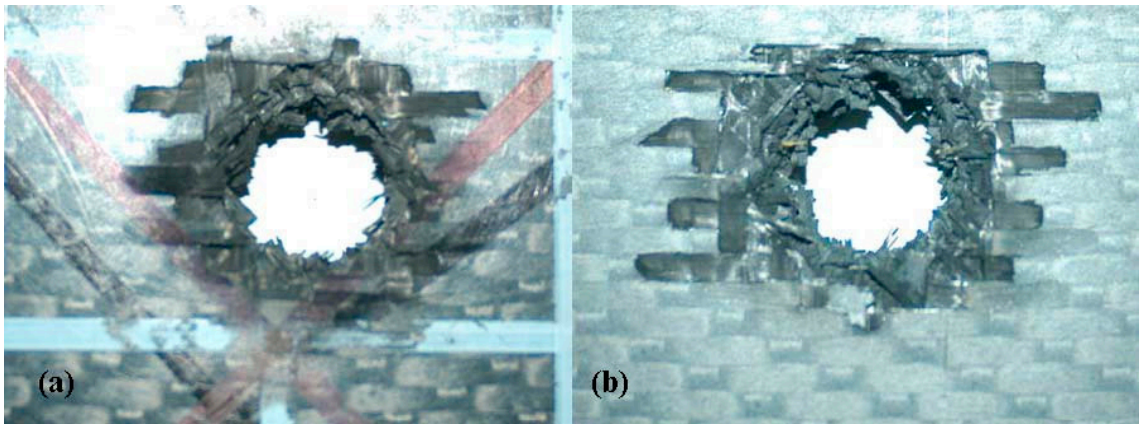

Figure 4. Post-impact images of 6 mm thick target plate in the vicinity of impact (A3): (**a**) impact face and (**b**) rear face.

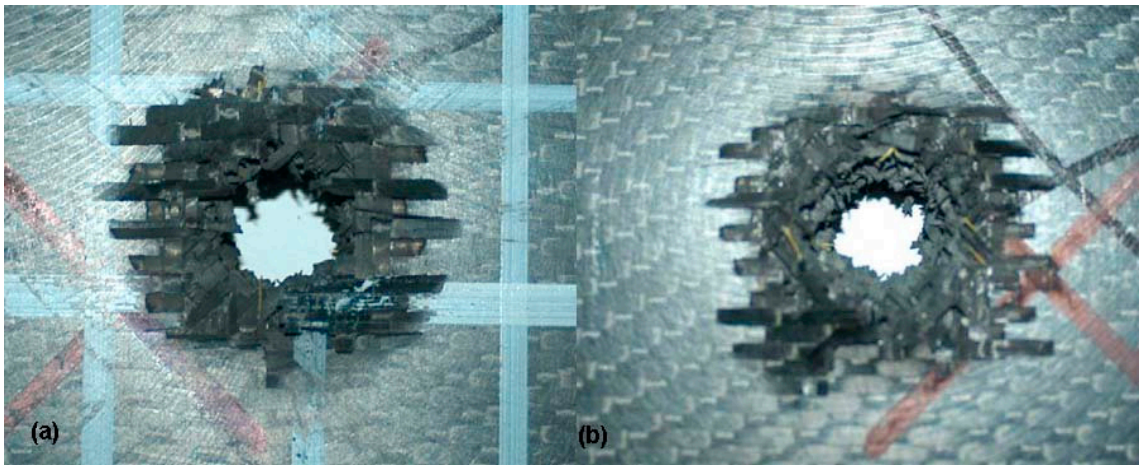

Figure 5. Post-impact images of 12 mm thick target plate in the vicinity of impact (C3): (**a**) impact face and (**b**) rear face.

4. Simulation Results

Two finite element models of a quarter of the sphere impact tests are shown in Figures 6 and 7. Two perpendicular symmetry planes were defined through the impact direction in terms of appropriate boundary conditions (x displacement constrained in x = 0 plane and y displacement constrained in y = 0 plane). High-velocity impact is driven by the local effects, and to reduce computational costs, the in-plane target dimensions of the FE model were smaller than the dimensions of the real specimens, with the transparent (non-reflecting) boundary conditions applied around the model edges. These boundary conditions do not affect the local physical process that drives deformation and failure of the target.

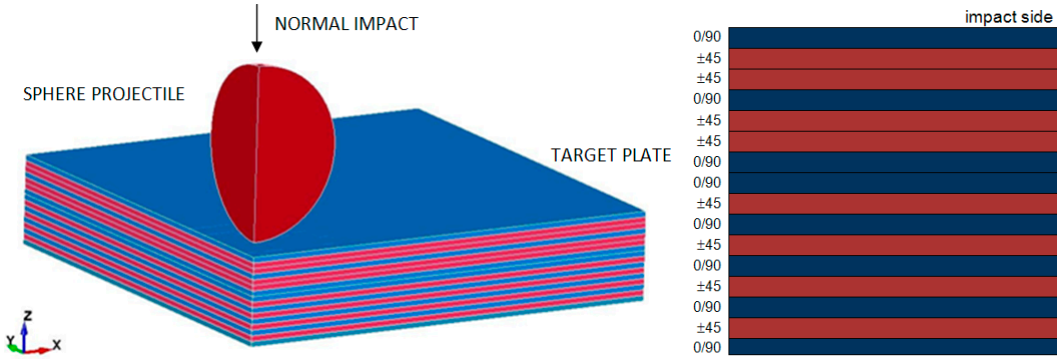

(**a**) (**b**)

Figure 6. (**a**) FEM model of a quarter of the sphere impact on woven CFRP composite target—6 mm thick target plate and (**b**) stack sequence of 6 mm thick woven CFRP composite plate.

In all FEM models, the CFRP target plate was modelled with three solid elements per thickness of the ply in order to capture delamination and bending of the plate properly. A quarter of the 6 mm target plate was modelled by 96,000 solid elements with one integration point, whilst a quarter of the sphere projectile was modelled with 4864 solid elements. The 12 mm thick plate, comprising 32 plies, was modelled with 192,000 solid elements.

The plate was modelled as a quasi-orthotropic material, with the material properties given in Tables 2 and 3. The Mie–Grüneisen EOS data are given in Table 4.

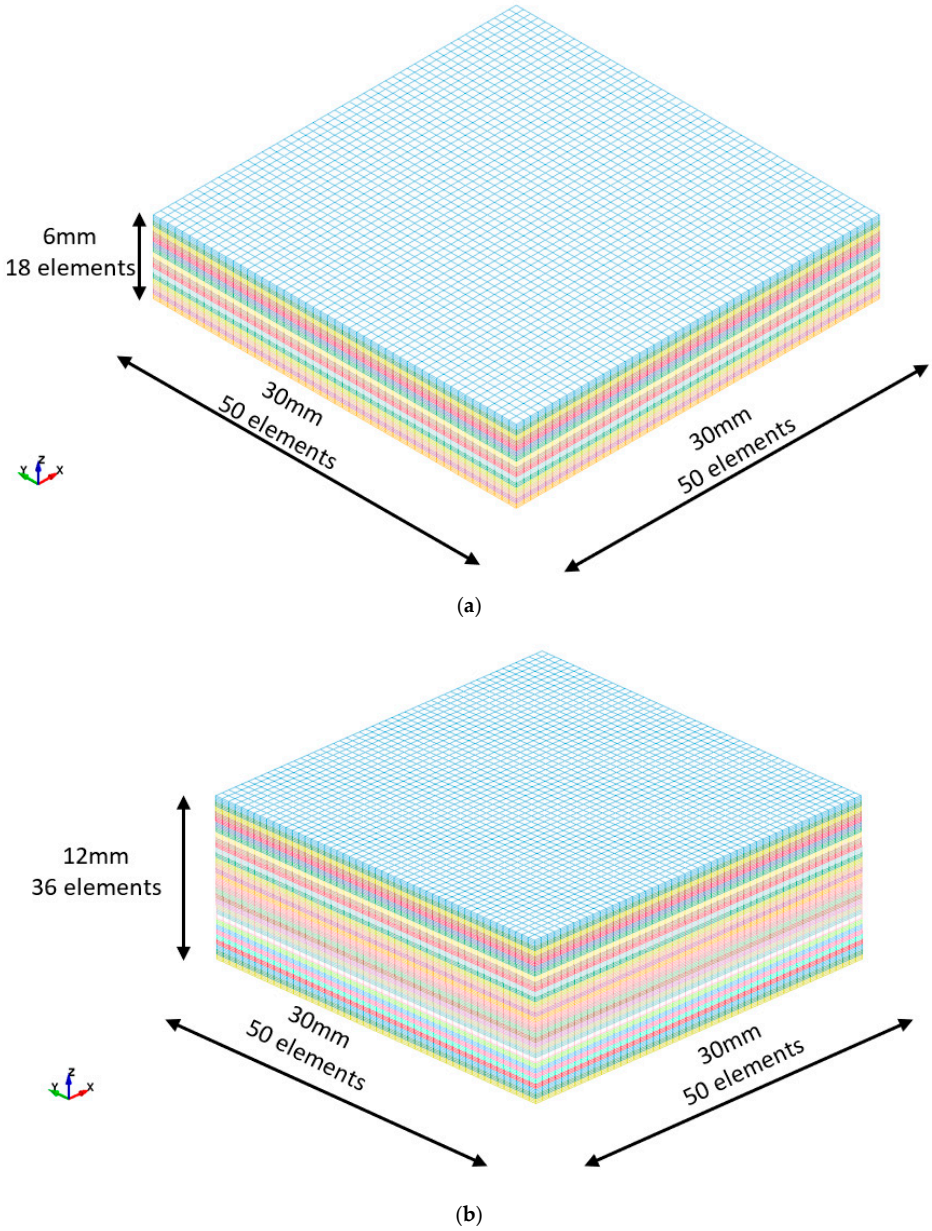

Figure 7. FEM models of a quarter of the CFRP target plates, were the different colors represent different plies: (**a**) 6 mm thick composite A3 and (**b**) 12 mm thick composite C3 modelled.

Table 2. Material elastic properties of woven carbon fibre composite [40].

Density	1500 kgm^{-3}
Elastic modulus in longitudinal direction E_a	68.465 GPa
Elastic modulus in longitudinal direction E_b	66.534 GPa
Elastic modulus in longitudinal direction E_c	10.0 GPa
Poisson's ratio υ_{ba}	0.0039
Poisson's ratio υ_{ca}	0.0044
Poisson's ratio υ_{cb}	0.0045
Shear modulus G_{ab}	4.57 GPa
Shear modulus G_{bc}	3.57 GPa
Shear modulus G_{ca}	3.57 GPa

Table 3. Parameters for composite damage model.

In-plane tensile strength in warp direction, aa	848.05 MPa
In-plane tensile stress fill direction, bb	806.68 MPa
In-plane compression strength in warp direction, aa	689.48 MPa
In-plane compression strength fill direction, bb	657 MPa
Critical tensile delamination stress	71.7 MPa
In-plane shear strength, ab	102.73 MPa
Interlaminar shear strength, ac, bc	71.7 MPa
Material constant for in-plane damage evolution, Ω	20 s^{-1}
Material constant for delamination evolution, Ω_{del}	20 s^{-1}

Table 4. Mie–Grüneisen EOS measured in the through thickness direction for CFRP composite [41].

Velocity curve intercept, c	3230 m/s
First slope coefficient, S_1	0.92
Grüneisen coefficient, γ_0	0.84
First-order volume correction coefficient, a	0.50

The simulation programme consisted of four simulations: (1) impact on 6 mm thick CFRP target plate at 194 m/s; (2) impact on 6 mm thick CFRP target plate at 354 m/s; (3) impact on 6 mm CFRP target plate at 1200 m/s and (4) impact on 12 mm CFRP target plate at 1219 m/s. These test cases were chosen to cover a range of velocities which correspond to different dominant damage/failure mechanisms.

The sphere, 12 mm in diameter, was fully annealed stainless steel with isotropic properties. It was modelled by using the Johnson–Cook material model (material 15 in DYNA3D [6]) with material properties given in Table 5.

Table 5. Material properties for SS304 steel sphere [42].

Density	7.923 g/cm^3
Shear modulus, G	77 GPa
A	340 MPa
B	500 MPa
m	1.0
N	0.35
Specific heat	423 J/kg K
Melting temperature	2380 K
Ambient temperature	293 K
D_i	0.0
Mie–Grüneisen EOS—Type 4	
Velocity curve intercept, c	4.57 km/s
First slope coefficient, S_1	1.29
Grüneisen coefficient, γ_0	1.93
First-order volume correction coefficient, a	0.5

The contact algorithm used in the simulation is SAND (Slide surfaces with Adaptive New Definitions), which is available in DYNA3D as contact type 11.

Simulation of the first impact case at 194 m/s revealed a damage area in all plies normal to the impact, elliptical in shape, similar to the experimental observations. The damage area in the FEM models was calculated as the sum of the areas of the sides of the fully failed elements for each individual ply. The experimental result was obtained from the image processing of the tomography data in the interface plane. A comparison of the simulation results through the thickness and the experimental results is given in Figure 8.

The simulation results agree well with the experimental observation, particularly in the top half (impact side) of the composite target. The constitutive model underestimated the size of the damaged area at the back of the target plate, which can be attributed to quasi orthotropic material properties. Consequently, the model was stiffer in the fibre directions, so that initiation of the dominant failure mechanism (fibre failure in tension) was delayed. Another explanation could be that the structural response of the plate is not as localised as for the higher impact velocities, so that boundary conditions contributed to the plate response and damage extent.

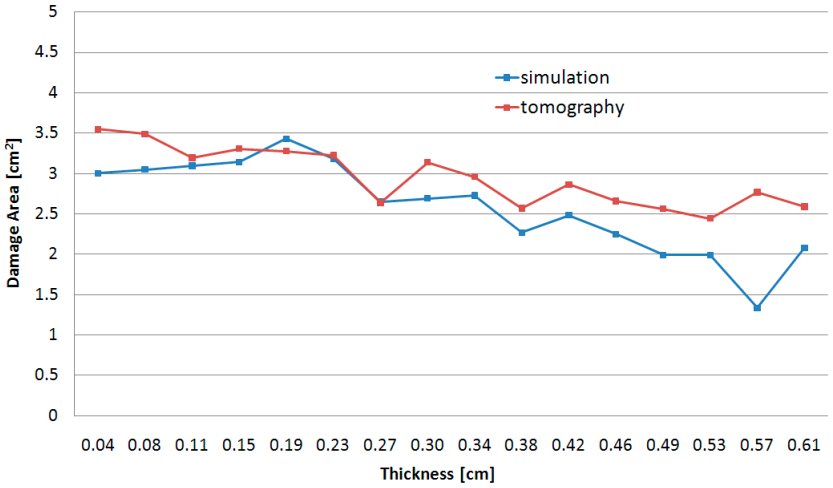

Figure 8. Damage area calculated from simulation results and XCT data for the normal impact at 194 m/s.

A similar comparison was conducted for the impact at 354 m/s (the shear-dominated failure mode); see Figure 9. The simulations predicted an increasing size of the damaged area through the thickness of the target plate, which suggests a conical shape of the damaged zone in the through thickness cross-section. And the shape agrees well with the experimental data. However, the constitutive model overestimated the magnitude of the damaged area in the top half of the target plate but shows a good agreement in the rear part of the target.

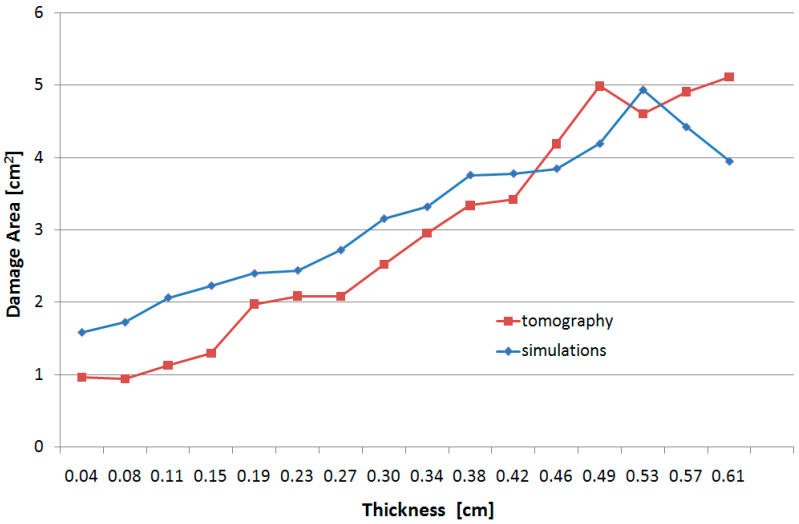

Figure 9. Damage area calculated from simulation results and XCT data for the normal impact at 354 m/s.

Simulation results for the impact at 1199 m/s are shown in Figures 10 and 11 and reported in Table 6. The latter consists of the hole diameters measured in two principal

material directions, denoted x_1 and x_2, and the size of the maximum visible delamination in two principal material directions on the impact side and the rear side, which are denoted with y_1 and y_2.

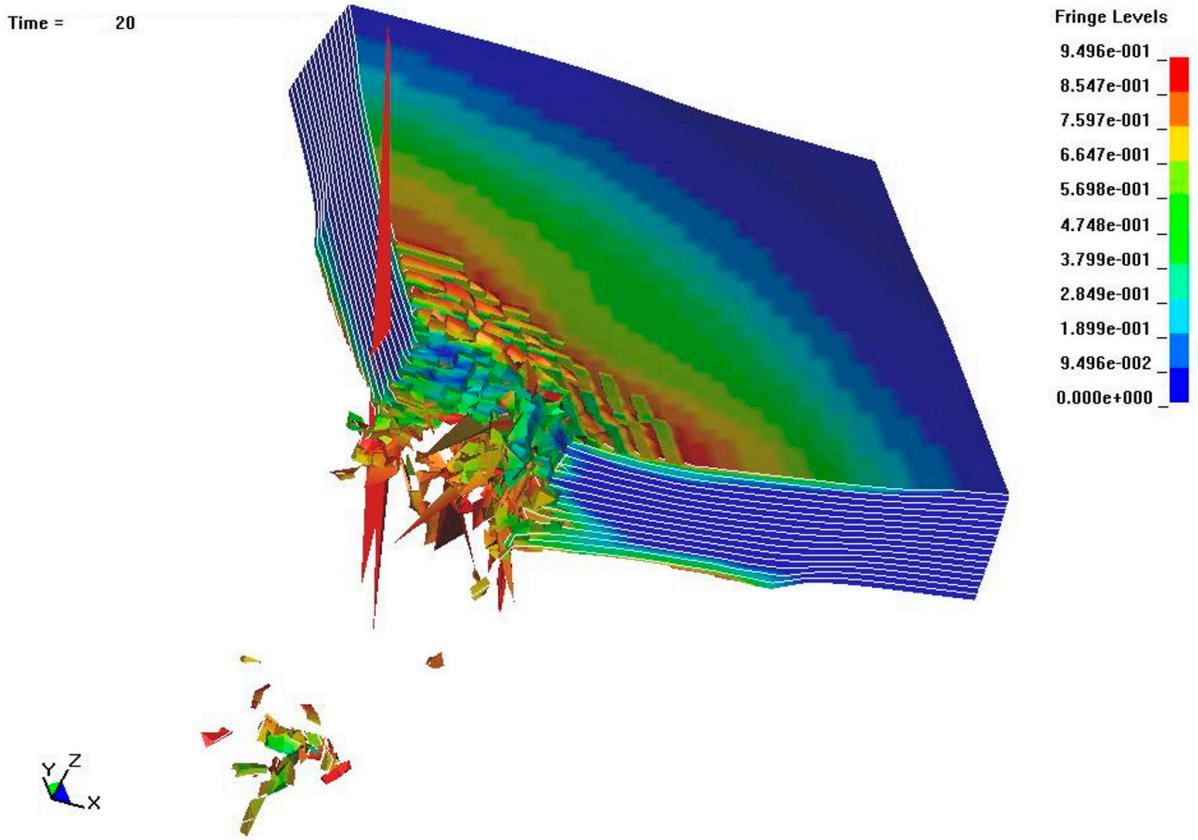

Figure 10. Simulation results for damage distribution in 6 mm thick CFRP after impact at 1199 m/s; t = 20 µs.

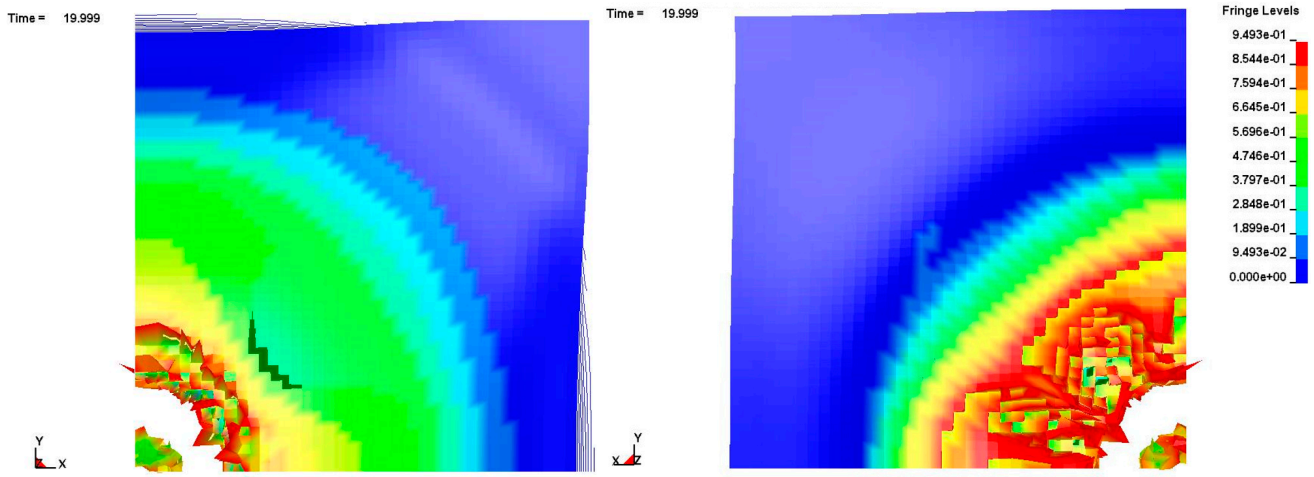

(**a**) (**b**)

Figure 11. Simulation results for damage distribution for impact at 1200 m/s in the 6 mm thick CFRP: at t = 20 µs: (**a**) the top and (**b**) bottom plies.

Table 6. Experimental C-scan measurements and simulation results for composite plate A3—6 mm.

				Impact Face		Rear Face	
	Velocity, v (m/s)	**x_1 (mm)**	**x_2 (mm)**	**y_1 (mm)**	**y_2 (mm)**	**y_1 (mm)**	**y_2 (mm)**
Measurement	1199	11.7	12.8	19.8	24.3	40.0	23.3
Simulation A3	1200	12.0	13.2	21.0	21.4	43.2	32.4
Error A3	n/a	2.6	3.1	6.1	11.9	8.0	39.1

Wide damage zone and delamination were obtained in the top and bottom plies of a target plate, resulting in an hourglass shape of the damaged zone in the cross-section of the target plate. This numerical result was compared to the post-impact C scans of the A3 specimen, as shown in Figure 12.

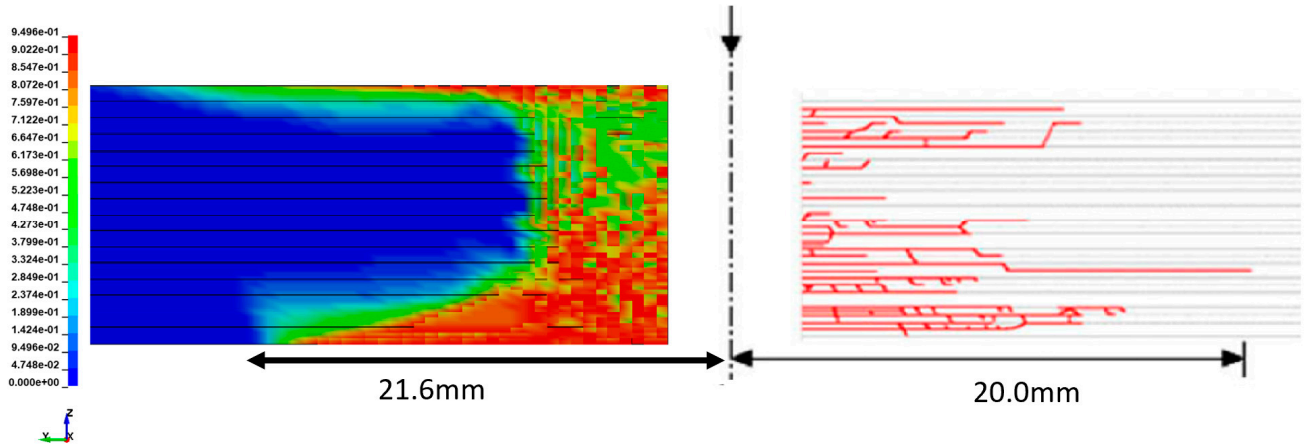

Figure 12. Damage distribution in 6 mm thick CFRP obtained in the simulation (**left**) and observed by C Scan (**right**) of the specimen after the impact at 1199 m/s.

The results compared well with the experimental observation in terms of the following:

- The calculated average diameter of the hole was within 4%.
- The hourglass shape of the delaminated zone was captured within the simulation.
- There was a bigger delamination zone at the back of the target plate in comparison to the front and the middle plies.
- The numerically obtained size of the delamination zone at the back of the target was within 8% of the experimental measures in the principal material direction.
- The model overestimated the size of the delamination zone in the minor material direction, particularly on the rear side of the plate.

The simulation results for impact at 1219 m/s on 12 mm thick CFRP target plate were also compared to the available experimental data, and reasonably good agreement was obtained in terms of the geometry of the hole, shape and dimensions of the delamination zone. The comparison is summarised in Table 7, whilst the simulation results are shown in Appendix A. The numerical results agree well with the experimental measurements, but for the size of the minor delamination axis on the impact size.

Table 7. Experimental C-scan measurements and simulation results for composite plate C3—12 mm.

				Impact Face		Rear Face	
	Velocity, v (m/s)	**x_1 (mm)**	**x_2 (mm)**	**y_1 (mm)**	**y_2 (mm)**	**y_1 (mm)**	**y_2 (mm)**
Measurement	1219	11.6	12.8	42.8	35.1	44.6	40.7
Simulation C3	1219	12.0	13.0	41.9	40.7	42.0	39.6
Error C3	n/a	3.4	1.6	2.1	16.0	5.8	2.7

5. Conclusions

The modelling of progressive damage in composite materials is still a challenging task, particularly when the material undergoes extreme loading, including shock. This paper presents a new constitutive model for orthotropic materials, developed in the framework of thermodynamics, where the damage evolution equations are based on a modified Tuler–Bucher criterion. Numerical results demonstrated the model capabilities to capture different damage modes developed in the material at different impact velocities above the plate ballistic limit. The prediction of the model with damage agreed well with experimental measurements, for both the size of the hole generated during the penetration and the size of the delamination zone. The simulation results were within 8% of the experimental measurements for all measurements, except the size of the delamination zone in the minor material direction. This may be due to delamination development within the material, which was not visible on the surface ply; see, for instance, Figure 11. This discrepancy may also be due to a number of uncertainties, including material properties and quality of manufacturing of the samples, and should be investigated further in future work.

Author Contributions: Conceptualization, N.D. and R.V.; methodology, N.D. and R.V.; software, N.D. and T.D.V.; validation, N.D. and K.H.; formal analysis, N.D., R.V., K.H. and T.D.V.; investigation, N.D. and R.V.; resources, R.V.; writing—original draft preparation, N.D. and R.V.; writing—review and editing, N.D., R.V., K.H. and T.D.V.; visualization, N.D., R.V. and K.H. All authors have read and agreed to the published version of the manuscript.

Funding: This research received no external funding.

Data Availability Statement: The data presented in this study are available on request from the corresponding author.

Acknowledgments: The authors would like to thank COST Action CA21155—Advanced Composites under HIgh STRAin RaTEs Loading: A route to certification-by-analysis HISTRATE.

Conflicts of Interest: The authors declare no conflicts of interest. The funders had no role in the design of the study; in the collection, analyses, or interpretation of data; in the writing of the manuscript; or in the decision to publish the results.

Appendix A

The simulation results for the damage distribution in a 12 mm thick CFRP composite target plate obtained in the impact of a sphere projectile at 1219 m/s at response time t = 35 μs are given in Figures A1–A3. The simulation results clearly suggest that the damage area is significantly larger than the impactor size on the top and rear surface, whilst it is almost minimum in the midsection of the target plate.

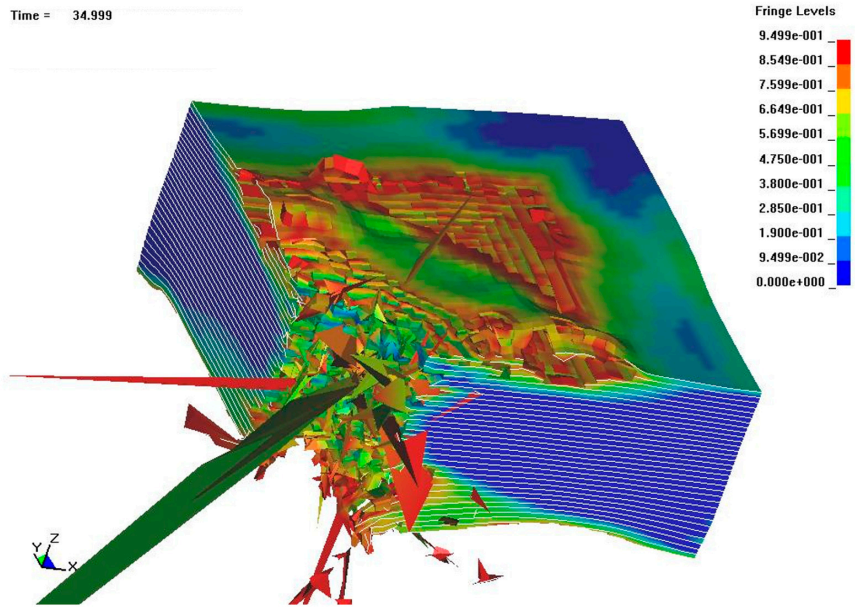

Figure A1. Damage distribution in 12 mm thick CFRP target plate C3 at response time t = 35 µs; 3 solid elements per layer.

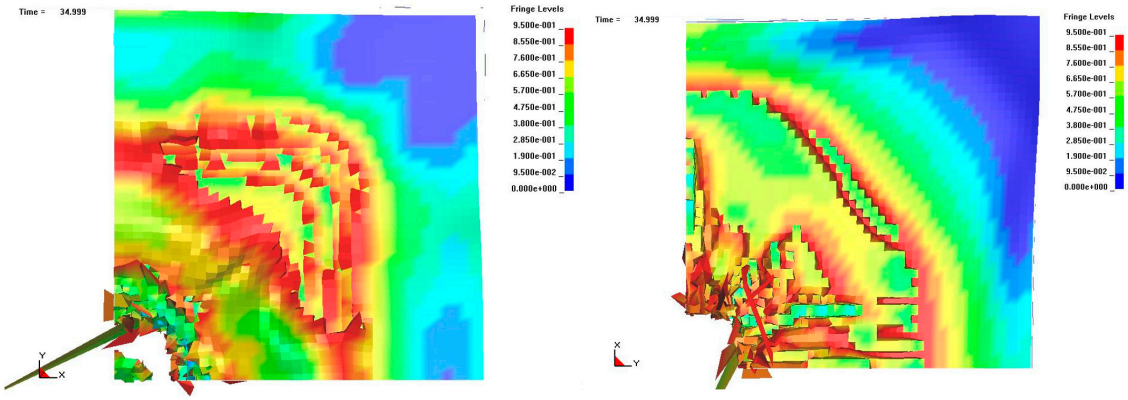

(**a**) (**b**)

Figure A2. Damage distribution in 12 mm thick CFRP target plate C3 at response time t = 35 µs: (**a**) impact side and (**b**) rear side.

Figure A3. Damage distribution in midplane of the 12 mm thick CFRP target plate C3 at response time t = 35 µs.

References

1. Tsai, S.W. *Composites Design*; Thick Composites: Dayton, OH, USA, 1985.
2. Tsai, S.W.; Wu, E.M. A General Theory of Strength for Anisotropic Materials. *J. Compos. Mater.* **1971**, *5*, 58–80. [CrossRef]
3. Chang, F.-K.; Chang, K.-Y. Post-Failure Analysis of Bolted Composite Joints in Tension or Shear-Out Mode Failure. *J. Compos. Mater.* **1987**, *21*, 809–833. [CrossRef]
4. Chang, F.-K.; Chang, K.-Y. A Progressive Damage Model for Laminated Composites Containing Stress Concentrations. *J. Compos. Mater.* **1987**, *21*, 834–855. [CrossRef]
5. Livermore Software Techology. *LS-Dyna. Livermore Software Technology (Lst)*; An Ansys Company: Livermore, CA, USA, 2021; 94551: R13.
6. Hallquist, J.O.; Lin, J.I. *DYNA3D: A Nonlinear, Explicit, Three-Dimensional Finite Element Code for Solid and Structural Mechanics User Manual*; Methods Development Group Mechanical Engineering, Lawrence Livermore National Laboratory: Livermore, CA, USA, 2005.
7. Orifici, A.C.; Herszberg, I.; Thomson, R.S. Review of methodologies for composite material modelling incorporating failure. *Compos. Struct.* **2008**, *86*, 194–210. [CrossRef]
8. Voyiadjis, G.Z.; Kattan, P.I. Damage of fiber-reinforced composite materials with micromechanical characterization. *Int. J. Solids Struct.* **1993**, *30*, 2757–2778. [CrossRef]
9. Voyiadjis, G.Z.; Kattan, P.I.; Taqieddin, Z.N. Continuum Approach to Damage Mechanics of Composite Materials with Fabric Tensors. *Int. J. Damage Mech.* **2007**, *16*, 301–329. [CrossRef]
10. Barbero, E.J.; de Vivo, L. A Constitutive Model for Elastic Damage in Fiber-Reinforced PMC Laminae. *Int. J. Damage Mech.* **2001**, *10*, 73–93. [CrossRef]
11. Hayakawa, K.; Murakami, S. Thermodynamical Modeling of Elastic-Plastic Damage and Experimental Validation of Damage Potential. *Int. J. Damage Mech.* **1997**, *6*, 333–363. [CrossRef]
12. Krajcinovic, D.; Lubarda, V.; Sumarac, D. Fundamental aspects of brittle cooperative phenomena—Effective continua models. *Mech. Mater.* **1993**, *15*, 99–115. [CrossRef]
13. Pinho, S.T.; Iannucci, L.; Robinson, P. Physically based failure models and criteria for laminated fibre-reinforced composites with emphasis on fibre kinking. Part II: FE implementation. *Compos. Part. A Appl. Sci. Manu* **2006**, *37*, 766–777. [CrossRef]
14. Pinho, S.T.; Iannucci, L.; Robinson, P. Physically based failure models and criteria for laminated fibre-reinforced composites with emphasis on fibre kinking. Part I: Development. *Compos. Part. A Appl. Sci. Manuf.* **2006**, *37*, 63–73. [CrossRef]
15. Maimí, P.; Camanho, P.P.; Mayugo, J.A.; Dávila, C.G. A continuum damage model for composite laminates: Part I–Constitutive model. *Mech. Mater.* **2007**, *39*, 897–908. [CrossRef]
16. Maimí, P.; Camanho, P.P.; Mayugo, J.A.; Dávila, C.G. A continuum damage model for composite laminates: Part II–Computational implementation and validation. *Mech. Mater.* **2007**, *39*, 909–919. [CrossRef]
17. Gama, B.A. User Manual: A Progressive Composite Damage Model For Unidirectional and woven fabric. *Energy Fuels* **2015**, *24*, 6533–6539. [CrossRef]
18. Zhao, L.; Li, Y.; Zhang, J.; Zhou, L.; Hu, N. A novel material degradation model for unidirectional CFRP composites. *Compos. B Eng.* **2018**, *135*, 84–94. [CrossRef]
19. Matzenmiller, A.; Lubliner, J.; Taylor, R.L. A constitutive model for anisotropic damage in fiber-composites. *Mech. Mater.* **1995**, *20*, 125–152. [CrossRef]
20. Haque, B.Z. A Progressive Composite Damage Model for Unidirectional and Woven Fabric Composites. In Proceedings of the 13th International LS-Dyna Users Conference, Detroit, MI, USA, 2014; Available online: https://www.ccm.udel.edu/wp-content/uploads/2014/12/MAT162-USER-MANUAL-Version-14C-2014.pdf (accessed on 1 December 2024).
21. Davila, C.G.; Camanho, P.P. *Failure Criteria for FRP Laminates in Plane Stress*; NASA/TM-2003-212663; NASA: Washington, DC, USA, 2003.
22. Zhang, J.; Zhou, L.; Chen, Y.; Zhao, L.; Fei, B. A micromechanics-based degradation model for composite progressive damage analysis. *J. Compos. Mater.* **2016**, *50*, 2271–2287. [CrossRef]
23. Puck, A.; Schürmann, H. Failure Analysis of FRP Laminates by Means of Physically Based Phenomenological Models. *Compos. Sci. Technol.* **1998**, *58*, 1045–1067. [CrossRef]
24. Gosse, J.; Christensen, S. Strain invariant failure criteria for polymers in composite materials. In Proceedings of the 19th AIAA Applied Aerodynamics Conference, Anaheim, CA, USA, 11–14 June 2001; American Institute of Aeronautics and Astronautics: Reston, VA, USA, 2001. [CrossRef]
25. Tay, T.E.; Tan, S.H.N.; Tan, V.B.C.; Gosse, J.H. Damage progression by the element-failure method (EFM) and strain invariant failure theory (SIFT). *Compos. Sci. Technol.* **2005**, *65*, 935–944. [CrossRef]
26. Rosenberg, Z.; Luttwak, G.; Yeshurun, Y.; Partom, Y. Spall studies of differently treated 2024A1 specimens. *J. Appl. Phys.* **1983**, *54*, 2147–2152. [CrossRef]
27. Tuler, F.R.; Butcher, B.M. A criterion for the time dependence of dynamic fracture. *Int. J. Fract. Mech.* **1968**, *4*, 431–437. [CrossRef]

28. Rubin, M.B. Analysis of weak shocks in 6061-T6 aluminum. In *Shock Compression of Condensed Matter: Proceedings of the American Physical Society Topical Conference, Albuquerque, NM, USA, 14–17 August 1989*; Schmidt, S.C., Johnson, J.N., Eds.; American Institute of Physics: New York, NY, USA, 1990.
29. Anderson, C.E.; Cox, P.A.; Johnson, G.R.; Maudlin, P.J. A constitutive formulation for anisotropic materials suitable for wave propagation computer programs—II. *Comput. Mech.* **1994**, *15*, 201–223. [CrossRef]
30. Vignjevic, R.; Campbell, J.C.; Bourne, N.K.; Djordjevic, N. Modeling shock waves in orthotropic elastic materials. *J. Appl. Phys.* **2008**, *104*, 044904. [CrossRef]
31. Gilman, J.J.; Tuler, F.R. Dynamic fracture by spallation in metals. *Int. J. Fract. Mech.* **1970**, *6*, 169–182. [CrossRef]
32. Krajcinovic, D. Continuous Damage Mechanics Revisited: Basic Concepts and Definitions. *J. Appl. Mech.* **1985**, *52*, 829–834. [CrossRef]
33. Hansen, N.R.; Schreyer, H.L. A thermodynamically consistent framework for theories of elastoplasticity coupled with damage. *Int. J. Solids Struct.* **1994**, *31*, 359–389. [CrossRef]
34. Naboulsi, S.K.; Palazotto, A.N. Elastic-Plastic Damage Model for Composites Under High Intensity Loading. *J. Thermoplast. Compos. Mater.* **2003**, *16*, 31–43. [CrossRef]
35. Cordebois, J.P.; Sidoroff, F. Damage Induced Elastic Anisotropy. In *Mechanical Behavior of Anisotropic Solids/Comportment Méchanique des Solides Anisotropes*; Springer: Dordrecht, The Netherlands, 1982; pp. 761–774. [CrossRef]
36. Sidoroff, F. Description of Anisotropic Damage Application to Elasticity. In *Physical Non-Linearities in Structural Analysis*; Springer: Berlin/Heidelberg, Germany, 1981; pp. 237–244. [CrossRef]
37. Kachanov, L.M. Time of the rupture process under creep conditions, Izy Akad. *Nank SSR Otd. Tech. Nauk.* **1958**, *8*, 26–31.
38. Krajcinovic, D. *Damage Mechanics*, 1st ed.; Elsevier Science: Amsterdam, The Netherlands, 1996; Volume 41.
39. Hazell, P.J.; Cowie, A.; Kister, G.; Stennett, C.; Cooper, G.A. Penetration of a woven CFRP laminate by a high velocity steel sphere impacting at velocities of up to 1875 m/s. *Int. J. Impact. Eng.* **2009**, *36*, 1136–1142. [CrossRef]
40. Campbell, K. *Material Characterisation 5HS/RTM 6, Report No. ELRIPS-WP7b-Bom-TREP-02, ELRPIS Project GR/S33956/01*; Bombardier Aerospace: Montreal, QC, Canada, 2004.
41. Millett, J.C.F.; Bourne, N.K.; Meziere, Y.J.E.; Vignjevic, R.; Lukyanov, A. The effect of orientation on the shock response of a carbon fibre–epoxy composite. *Compos. Sci. Technol.* **2007**, *67*, 3253–3260. [CrossRef]
42. Steinberg, D.J. *Equation of State and Strength Properties of Selected Materials*; UCRL-MA-106439; Laurence Livermore National Laboratory: Livermore, CA, USA, 1996.